

# On the nature of the QCD chiral phase transition with imaginary chemical potential

Alfredo D'Ambrosio<sup>\*1,2</sup>, Michael Fromm<sup>†1</sup>, Reinhold Kaiser<sup>‡1,2</sup>, and Owe Philipsen<sup>§1,2</sup>

<sup>1</sup> Institute for Theoretical Physics, Goethe-Universität Frankfurt, Max-von-Laue-Str. 1, 60438 Frankfurt am Main, Germany

<sup>2</sup> John von Neumann Institute for Computing (NIC), GSI Helmholtzzentrum für Schwerionenforschung, Planckstr. 1, 64291 Darmstadt, Germany

## Abstract

The order of the thermal chiral phase transition in lattice QCD is known to be strongly cutoff-dependent. A previous study using  $N_f \in [2, 6]$  mass-degenerate, unimproved staggered quark flavours on  $N_\tau \in \{4, 6, 8\}$  lattices found that the bare mass regions displaying explicit first-order transitions shrink to zero, with their critical boundary line terminating in a tricritical point before the continuum limit is reached. Here we perform an analogous study for fixed imaginary baryon chemical potential and find the same behaviour: first-order regions observed on coarse lattices disappear in tricritical points with diminishing lattice spacing. These observations are consistent with currently available results from improved staggered discretisations, both at zero and non-zero imaginary chemical potential. Unless additional first-order transitions are found on finer lattices or with chiral lattice actions, this implies a second-order transition in the continuum chiral limit for all these cases, at zero and imaginary chemical potential. Ultimately, implications for the  $N_f = 2 + 1$  QCD phase diagram at the physical point are discussed.

## 1 Introduction

The chiral limit of QCD, corresponding to massless quarks, is crucial for our understanding of the strong interactions, because the physical  $u, d$ -quarks represent a small distortion of that situation. A natural question then is how the chiral crossover observed at physical quark masses [1] emerges from a necessarily non-analytic chiral phase transition in the limit  $m_{u,d} \rightarrow 0$ . Furthermore, the nature of the chiral phase transition in the massless limit constrains the phase diagram of physical QCD at finite temperature  $T$  and baryon chemical potential  $\mu_B$  [2, 3, 4, 5, 6, 7]. Lattice QCD in the chiral limit cannot be simulated directly, because fermion matrix inversion becomes singular in that case. Therefore, extrapolations of simulation sequences with decreasing quark masses are necessary. Despite these difficulties, decisive progress has been achieved over the last few years, as we now summarise.

The quark mass dependence of the pseudo-critical crossover temperature appears to be only weakly sensitive to the precise set of critical exponents, with which the chiral limit is approached, or even to the order of the transition. This allows for stable extrapolations  $m_{u,d} \rightarrow 0$  at the physical strange quark mass, leading to  $T_c(m_{u,d} = 0, m_s^{\text{phys}}) = 132_{-6}^{+3}$  MeV when using highly improved staggered (HISQ) fermions [8], and  $T_c(m_{u,d} = 0, m_s^{\text{phys}}) = 134_{-4}^{+6}$  MeV when using twisted mass Wilson fermions [9].

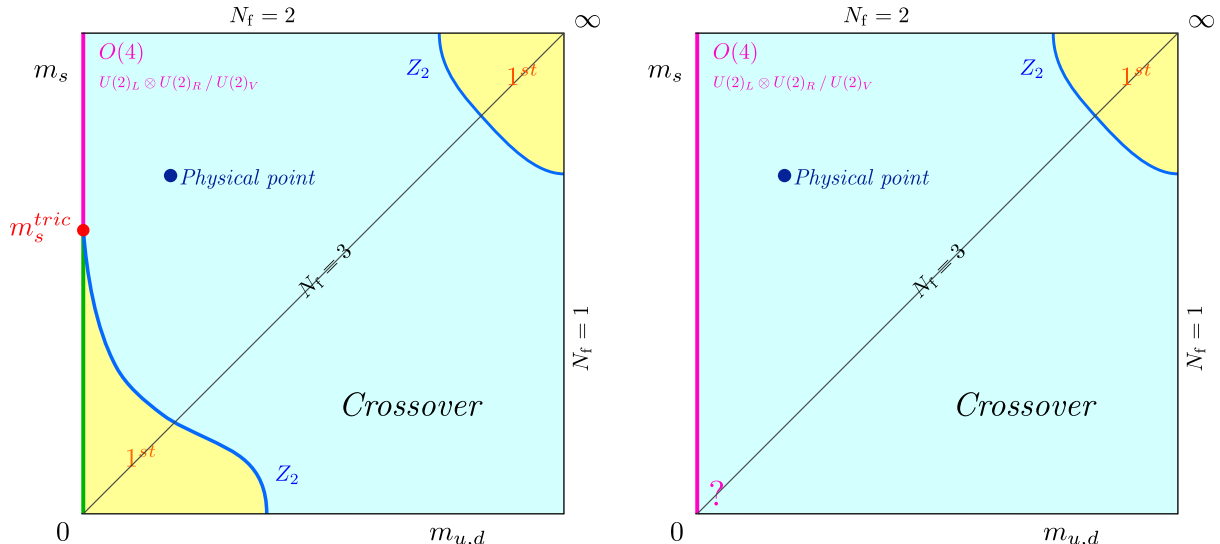
---

\*ambrosio@itp.uni-frankfurt.de

†mfromm@itp.uni-frankfurt.de

‡kaiser@itp.uni-frankfurt.de

§philipsen@itp.uni-frankfurt.de



(a) Prediction by 3d  $\phi^4$ -theories, augmented by a 't Hooft determinant [10, 11]. Figure taken from ref. [12]. (b) Prediction by lattice QCD with standard staggered fermions [12], consistent with all presently available lattice results. Figure taken from ref. [12].

Figure 1: Nature of the  $N_f = 2 + 1$  QCD thermal transition as a function of quark masses. Figures taken from [12].

By contrast, it is much harder to obtain robust lattice results on the order of the chiral transition because of the necessary finite size scaling analysis, in addition to the continuum and chiral extrapolations. For  $N_f = 2 + 1$  QCD, the nature of the thermal transition as a function of quark masses is schematically represented in the so-called Columbia plot, figures 1a and 1b. For more than 30 years, the version displayed in figure 1a was expected to be realised by QCD, based on renormalisation group (RG) flows in linear sigma models [10, 13, 14, 11] and early numerical results obtained on coarse lattices [15, 16]. However, the chiral critical  $Z_2$ -line [17, 18] delimiting the first-order region was found to be strongly cutoff-dependent, with enormous apparent differences between different lattice actions, see [19, 20, 21] for reviews and references.

A resolution was suggested by mapping out the chiral critical boundary between first-order and crossover regions in an enlarged multi-flavour parameter space using unimproved<sup>1</sup> staggered fermions [12]. All theories with  $N_f \in [2, 6]$  mass-degenerate flavours exhibit a first-order chiral transition region on coarse  $N_\tau = 4$  lattices, which shrinks with increasing  $N_\tau$  (viz. decreasing lattice spacing) to disappear in a tricritical point, before the continuum limit is reached. This implies that the continuum chiral limit corresponds to a second-order transition for all these cases. Complementary to this, a re-analysis of previously published data for  $N_f = 3$   $\mathcal{O}(a)$ -improved Wilson fermions [22] was also found to be consistent with tricritical scaling and thus a second-order transition in the continuum limit [12]. Unless an additional first-order region emerges in future simulations on finer lattices or with chiral fermions, these results suggest a continuum Columbia plot as in figure 1b. Note that currently nothing is known about the universality class in the lower left  $N_f = 3$  corner, whose classical chiral symmetry is  $U(3) \times U(3)$ .

Since a  $N_f = 3$  second-order transition differs qualitatively from earlier predictions, independent checks are crucial. Investigations of the  $N_f = 3$  theory with two further discretisations are also consistent with these results: no sign of a first-order phase transition is detected with HISQ fermions down to  $m_\pi \approx 45\text{MeV}$  [23], nor with domain wall fermions at a mass value

<sup>1</sup>The primary interest of our studies is to understand cutoff effects on the order of the phase transition. It is therefore beneficial to work with a discretisation that displays them clearly.

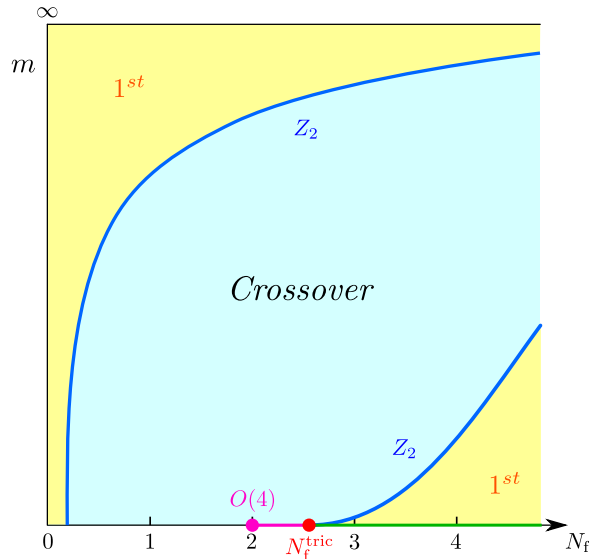


Figure 2: Columbia plot for mass-degenerate quarks, scenario analogous to figure 1a. Figure taken from ref. [12].

of the physical  $u, d$ -quarks [24, 25, 26]. In ref. [27] the RG flow of a three-dimensional  $\phi^6$ -theory was studied with functional methods, finding an infrared fixed point as a candidate for a second-order transition, depending on the fate of the  $U(1)_A$  anomaly at the transition temperature. Conditions on the anomaly permitting a second-order transition are also formulated in [28, 29]. A similar RG analysis predicts second-order transitions for  $N_f \geq 5$  independent of the anomaly [30]. Numerical conformal bootstrap methods provide evidence for the possibility of a second-order transition in generic  $U(3) \times U(3)$  models [31]. A second-order chiral transition is also reported in  $N_f = 2 + 1$  QCD for all strange quark mass values using truncated Dyson-Schwinger equations (DSE) of continuum QCD, where the massless limit can be studied explicitly [32].

In this paper we continue to study the predictions of standard staggered fermions, and investigate how the order of the chiral phase transition depends on baryon chemical potential  $\mu_B$ . As a first step, we repeat the analysis of ref. [12] for a fixed imaginary chemical potential, for which there is no sign problem. The emerging qualitative picture is completely analogous to the situation at  $\mu_B = 0$ : while a first-order phase transition region is explicitly seen on coarse  $N_\tau = 4$ -lattices [18], it shrinks with diminishing lattice spacing to disappear in a tricritical line.<sup>2</sup> Again this is consistent with the picture from DSE studies [32, 34], where the nature of the chiral transition was found to be independent of imaginary or small real chemical potentials. Moreover, the DSEs in their current truncation explicitly demonstrate analyticity of the chiral critical surface around  $\mu_B = 0$ , thus further motivating lattice studies at imaginary chemical potentials.

## 2 The Columbia plot at zero and imaginary chemical potential

To render this paper self-contained, we briefly summarise the theoretical concepts for our numerical strategy, which have been first proposed and discussed in more detail in refs. [35, 12]. Instead of  $N_f = 2 + 1$  QCD we consider a parameter space with a continuously variable number  $N_f$  of mass-degenerate quarks with bare mass  $m$ . Just as the strange quark mass  $m_s \in [m_{u,d} = m, \infty)$  interpolates between theories with  $N_f = 3$  or  $N_f = 2$  flavours of mass  $m$ , respectively, so does a continuous variation of the power  $N_f \in [2, 3]$ , to which the quark determinant is raised in the

<sup>2</sup>Preliminary evidence has been given in ref. [33].

QCD path integral,

$$Z(N_f, g, m) = \int \mathcal{D}A_\mu (\det M[A_\mu, m])^{N_f} e^{-S_{\text{YM}}[A_\mu]} . \quad (1)$$

Such a mapping  $\{m_{u,d}, m_s\} \rightarrow \{m, N_f\}$  is not unique, but that is not important for our purposes. In practice, we work with rooted staggered fermions where the desired roots can be straightforwardly adapted. The Columbia plot version from figure 1a then changes to figure 2, which features several advantages:

- Any first-order transition region observed at sufficiently large  $N_f$  must disappear in a tricritical point  $N_f^{\text{tric}}$ , because there is no chiral phase transition for integer  $N_f < 2$ .
- The  $Z_2$  boundary line delimiting the first-order transition region then represents a so-called wing line, which enters the tricritical point as a function of the symmetry breaking scaling field with known mean-field exponents [36],

$$N_f^c(m) = N_f^{\text{tric}} + A \cdot m^{2/5} + B \cdot m^{4/5} . \quad (2)$$

Starting from a known  $Z_2$  boundary point, one can map out the chiral critical line towards smaller masses and extrapolate it in a controlled way to determine the location of  $N_f^{\text{tric}}$ . One would then conclude that all integer  $N_f > N_f^{\text{tric}}$  feature first-order and all integer  $N_f < N_f^{\text{tric}}$  feature second-order chiral transitions.

On the lattice, the parameter space gets enlarged by the lattice spacing. Hence, the  $Z_2$ -boundary separating first-order transitions from crossover represents a surface, which in the lattice chiral limit ( $am = 0$ ) terminates in a tricritical line  $N_f^{\text{tric}}(a)$ . Using  $T = (aN_\tau)^{-1}$ , this can be expressed as  $N_f^{\text{tric}}(N_\tau)$ . In refs. [35, 12] this line was bounded in the space of  $N_f \in [2, 6]$  and  $N_\tau \in \{4, 6, 8\}$ . The results imply a possible tricritical point in the continuum to be at  $N_f^{\text{tric}}(N_\tau \rightarrow \infty) > 6$ . Inverting this relationship to  $N_\tau^{\text{tric}}(N_f)$ , one can restrict to the physical case of integer  $N_f$  again. The statement then is that for  $N_f \in [2, 6]$  there exists a finite  $N_\tau^{\text{tric}}(N_f) < \infty$ . This means that the first-order chiral transition is not analytically connected to the continuum limit, which then represents a second-order transition. Returning to the  $N_f = 2 + 1$  situation, one thus arrives at the continuum scenario displayed in figure 1b.

In the presence of a quark chemical potential,  $\mu = \mu_B/3$ , the Columbia plot (in the continuum or at fixed lattice spacing) gets extended into a third dimension. In this case the  $Z_2$ -critical boundary lines sweep out critical surfaces, as sketched schematically in figure 3, which depicts the situation found on coarse lattices. Labelling the third axis by  $(\mu/T)^2$ , both real and imaginary chemical potential can be discussed. Imaginary chemical potential,  $\mu = i\mu_i$  with  $\mu_i \in \mathbb{R}$ , is unphysical, but it does not induce a sign problem and the phase structure can be simulated without difficulty or further approximations. For arbitrary fermion masses the partition function is periodic in  $\mu_i$  according to the global Roberge-Weiss (or center) symmetry [37],

$$Z\left(T, i\frac{\mu_i}{T}\right) = Z\left(T, i\frac{\mu_i}{T} + i\frac{2\pi n}{N_c}\right) . \quad (3)$$

The boundaries between different center sectors are located at

$$(\mu/T)_c = \pm i(2n + 1)\pi/3 , \quad (4)$$

with  $n = 0, 1, 2, \dots$ , with the bottom plane of figure 3 representing the first of these. All adjacent sectors are related to the first one by symmetry.

For unimproved Wilson [40, 41] and staggered [42, 43, 39] discretisations on  $N_\tau \in \{4, 6\}$ , the 3D Columbia plot looks as in figure 3, with the region of chiral phase transitions getting wider

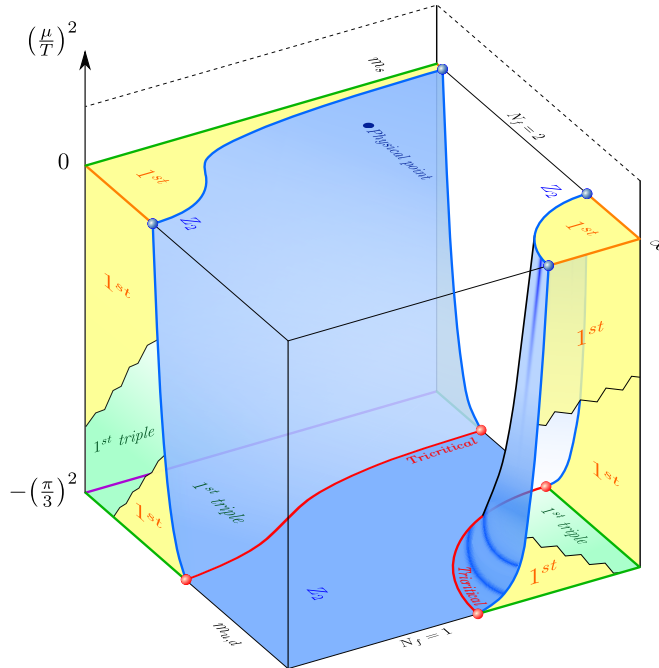


Figure 3: Columbia plot with chemical potential as observed on coarse lattices. The bottom plane corresponds to the first Roberge-Weiss center-transition [37]. Taken from [38, 39].

in the imaginary  $\mu$  direction. Expanding the  $Z_2$ -critical light mass for small chemical potential for any fixed  $m_s$ ,

$$\frac{m_l^c(\mu)}{m_l^c(0)} = 1 + c_1 \left(\frac{\mu}{T}\right)^2 + \mathcal{O}\left(\left(\frac{\mu}{T}\right)^4\right), \quad (5)$$

one may conclude that  $c_1 < 0$  and by analytic continuation the first order region shrinks in the real- $\mu$  direction. As an independent check on these calculations at imaginary chemical potential, the curvature of the chiral critical surface can be computed directly at  $\mu = 0$ . For staggered fermions one finds  $c_1 < 0$  both at  $m_s = m_l$  and at  $m_s = m_s^{\text{phys}}$ , and the next coefficient is negative as well [44, 45, 46]. The only calculation finding a positive curvature so far is based on  $\mathcal{O}(a)$ -improved Wilson fermions [47].

Investigations in the Roberge-Weiss plane on finer lattices reveal the same trend as seen at  $\mu = 0$ , namely the chiral tricritical line moving towards smaller quark masses, both for unimproved staggered [39] and Wilson [41] quarks. On the other hand, for stout-smearred staggered [48] and HISQ [49] actions, a first-order region in the Roberge-Weiss plane cannot be detected even on  $N_\tau = 4$ , when starting from the physical point and reducing the pion masses down to  $m_\pi \approx 50$  MeV.

In the following sections, we study how the  $Z_2$  boundary of the first-order transition region at imaginary chemical potential changes as a function of  $N_f$  and the lattice spacing using unimproved staggered fermions, i.e., we repeat the analysis of ref. [12] for a fixed chemical potential of  $\mu_i = 0.81\pi T/3$ .

### 3 Lattice simulations and analysis

For all Monte Carlo simulations we used the standard Wilson plaquette action for the gauge sector and the unimproved staggered action for the fermion sector. Gauge configurations were generated with the code `CL2QCD` version v1.1 [50], which employs the RHMC algorithm for degenerate quark flavors. The multiple pseudo-fermion technique was used to reduce the noise from stochastic estimates of the fermion determinant, with the optimal number of pseudo-

Table 1: Fit results for the critical quark mass and the associated gauge coupling.

$N_\tau$	$N_f$	$am_{\min}$	$am_{\max}$	$am_c$	fit type	d.o.f.	$\chi_{\text{d.o.f.}}^2$	$\beta_c$ at $am_c$
4	1.8	0.0014	0.0050	0.0023(8)	linear+corr	13	0.34	5.3162(13)
	1.9	0.0020	0.0060	0.0032(5)	linear	6	0.13	5.3007(8)
	2.0	0.0040	0.0120	0.0054(6)	linear	7	0.26	5.2879(11)
	2.1	0.0060	0.0130	0.0079(6)	linear	7	0.20	5.2757(11)
	2.2	0.0080	0.0140	0.0098(6)	linear	7	0.43	5.2628(11)
	2.3	0.0065	0.0230	0.0126(5)	linear	9	0.59	5.2517(9)
	3.6	0.0370	0.0520	0.0494(11)	linear+corr	9	0.24	5.1315(20)
	4.0	0.0500	0.0650	0.0596(10)	linear+corr	9	0.08	5.0993(18)
	4.5	0.0650	0.0750	0.0731(11)	linear+corr	6	0.19	5.0635(20)
	5.0	0.0750	0.1050	0.0872(11)	linear+corr	9	0.23	5.0324(20)
	6.0	0.1000	0.1300	0.1119(12)	linear+corr	6	0.04	4.9732(23)
6	3.0	0.0010	0.0030	0.0021(3)	linear+corr	5	0.79	5.2292(13)
	3.3	0.0030	0.0075	0.00433(20)	linear+corr	9	0.25	5.1877(9)
	3.6	0.0050	0.0100	0.0069(3)	linear+corr	6	0.15	5.1490(13)
	4.0	0.0075	0.0125	0.0107(3)	linear+corr	6	0.31	5.1010(14)
	4.5	0.0100	0.0180	0.0151(4)	linear+corr	6	0.95	5.0425(16)
	5.0	0.0175	0.0250	0.02082(25)	linear+corr	6	0.59	4.9913(10)
	6.0	0.0300	0.0380	0.0320(4)	linear+corr	6	0.60	4.8960(14)
8	4.0	0.0010	0.0030	0.00164(26)	linear+corr	8	0.66	5.1122(18)
	4.5	0.0020	0.0040	0.00309(18)	linear+corr	5	0.11	5.0367(14)
	5.0	0.0040	0.0075	0.00499(17)	linear+corr	8	0.98	4.9676(12)
	5.5	0.0050	0.0075	0.00663(17)	linear+corr	5	0.23	4.8990(12)
	6.0	0.0060	0.0100	0.00879(19)	linear+corr	5	0.01	4.8359(13)

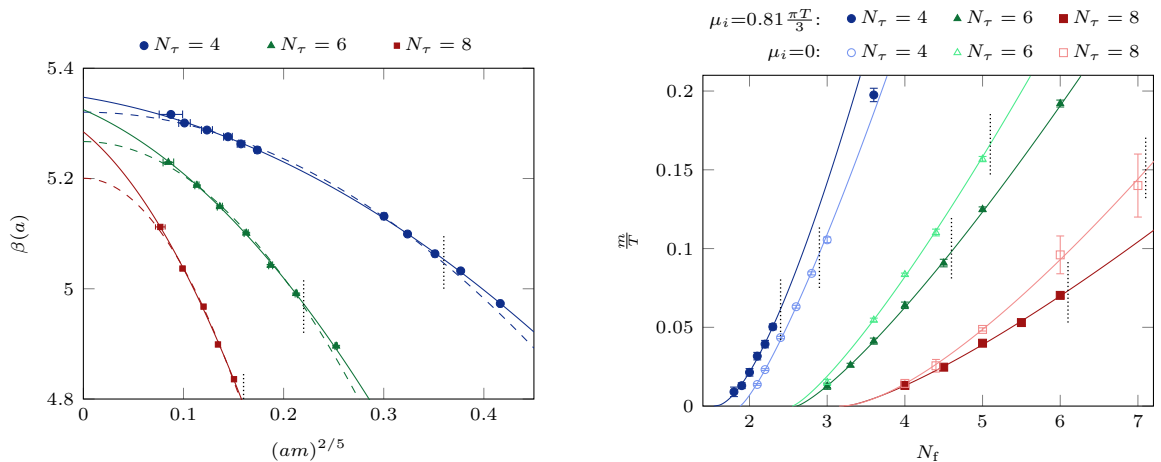
fermions calculated by  $\text{CI}^2\text{QCD}$  at the beginning of a run. The simulations were run on the Virgo cluster at GSI (Darmstadt) on AMD GPUs of type MI100, and monitored efficiently using the bash-software BaHaMAS [51]. In total almost 150 million trajectories have been generated, spread about 600 different parameter sets. For each parameter set, four differently seeded Markov chains were run independently to increase statistics. Our analysis follows the same steps as in ref. [12].

In order to determine the location and order of the chiral transitions, we use the chiral condensate as (quasi-)order parameter  $O = \bar{\psi}\psi$ , which we measure for each trajectory using 16 stochastic estimators. We then analyse its generalised moments,

$$B_n(\beta, am, N_\sigma) = \frac{\langle (O - \langle O \rangle)^n \rangle}{\langle (O - \langle O \rangle)^2 \rangle^{n/2}}. \quad (6)$$

When calculating the higher moments of the  $\bar{\psi}\psi$ , the bias subtraction method is applied, which prevents estimators of the  $\bar{\psi}\psi$  being multiplied with themselves.

In the four dimensional parameter space spanned by the lattice gauge coupling  $\beta$ , the quark mass  $am$ , the number of quark flavors  $N_f$  and the temporal lattice extent  $N_\tau$ , the chiral first-order region is separated from the crossover region by a  $Z_2$ -second-order surface. In practice we first scan in the lattice gauge coupling to determine the (pseudo-)critical hyper-surface (the ‘‘phase boundary’’) defined by vanishing skewness,  $B_3(\beta_{\text{pc}}, am, N_\sigma) = 0$ , and then employ the kurtosis evaluated on the phase boundary,  $B_4(\beta_{\text{pc}}, am, N_\sigma)$  in order to identify the chiral critical  $Z_2$ -surface in this subspace. In order to gain precision for  $\beta_{\text{pc}}$ , we interpolate both



(a)  $\beta_c$  as function of the rescaled bare quark mass  $(am)^{2/5}$  for several staggered flavors  $N_f$  at varying temporal extent  $N_\tau$ . The tricritical scaling fit (eq. (8) and table 2) includes LO+NLO (solid) and NLO (dashed) terms, respectively.

(b) The critical curves in the plane spanned by the quark mass and  $N_f$ . Fits correspond to eq. (9) with the fit results in table 3. Comparison between the data from  $\mu_i = 0$  [12] and  $\mu_i = 0.81 \pi T/3$ .

Figure 4: Projections of the critical surface on the  $(\beta, am)$ -plane (left) and on the  $(N_f, m/T)$ -plane (right).

standardized moments between the simulated  $\beta$ -values according to the multiple histogram method [52]. The  $Z_2$ -critical mass is identified by the kurtosis assuming its associated critical value of  $B_4^{Z_2} = 1.6044(10)$  [53]. In practice, we fit the kurtosis in the neighbourhood of the critical mass value to a finite size scaling formula,

$$B_4(\beta_{pc}, am, N_\sigma) \approx \left(1.6044 + c(am - am_c)N_\sigma^{1/\nu}\right) (1 + bN_\sigma^{y_t - y_h}), \quad (7)$$

which gives the critical mass  $am_c$  as a fit parameter. The last factor on the right hand side of eq. (7) contains a finite volume correction term, where  $y_t = 1/\nu = 1.5870(10)$  and  $y_h = 2.4818(3)$  [54] are the associated 3D Ising exponents. This term becomes statistically insignificant for sufficiently large volumes.

The values we obtained for the critical mass and coupling,  $am_c$  and  $\beta_c$ , respectively, are reported in table 1, which also includes fitting details. The value of  $\beta_c$  is obtained from a linear fit of the pseudo-critical  $\beta$ -values at the simulated quark masses. Evaluating the obtained fit function also at  $am_c \pm \sigma_{am_c}$  leads to the attached error of  $\beta_c$ . A detailed overview of the statistics associated to the results from table 1 are given in appendix A.

## 4 Results

The simulations and analysis described in the previous section provides us with the location of the chiral critical surface in the bare parameter space  $\{\beta, am, N_f, N_\tau\}$  of standard staggered fermions, with fixed  $\mu_i = 0.81\pi T/3$ . We will now project this critical surface on planes defined by different variable pairings and discuss the implications.

Beginning in the  $(\beta, am)$ -plane, figure 4a shows the  $Z_2$ -critical boundary line separating the parameter region with crossover to the right of it from the first-order region to the left of it, for lattices with different  $N_\tau$ . The different data points are implicitly parametrised by different values of  $N_f$ , which is increasing from left to right. No difference between integer and non-integer  $N_f$ -values is discernible. The lines show fits to leading and next-to-leading order in the tricritical scaling field. For all three  $N_\tau$ -values, the critical curves are well described over a



Table 2: Fits of eq. (8) to the data in figure 4a.

$N_\tau$	$\mathcal{C}_2$	$\mathcal{C}_1$	$\beta_{\text{tric}}$	range in $am$	fit form	d.o.f.	$\chi_{\text{d.o.f.}}^2$
4	-1.43(15)	-0.30(7)	5.347(7)	[0, 0.08]	LO+NLO	6	0.494
	-2.11(5)	—	5.3204(24)	[0, 0.08]	NLO	7	3.02
6	-3.7(1.0)	-0.8(3)	5.325(24)	[0, 0.03]	LO+NLO	3	0.623
	-6.17(14)	—	5.267(4)	[0, 0.03]	NLO	4	1.65
8	-10(6)	-1.5(1.5)	5.28(9)	[0, 0.01]	LO+NLO	2	0.834
	-16.3(6)	—	5.200(10)	[0, 0.01]	NLO	3	0.860

 Table 3: Fits of eq. (9) to the data for  $\mu_i = 0.27\pi T$  in figure 4b.

$N_\tau$	$\mathcal{D}_2(N_\tau)$	$\mathcal{D}_1(N_\tau)$	$N_f^{\text{tric}}$	range in $am$	fit form	d.o.f.	$\chi_{\text{d.o.f.}}^2$
4	13(8)	2.1(2.2)	1.54(15)	[0, 0.015]	LO+NLO	3	0.316
6	54(10)	0.0(2.6)	2.61(17)	[0, 0.018]	LO+NLO	2	0.345
8	11(4) · 10 <sup>1</sup>	2(9)	3.2(5)	[0, 0.01]	LO+NLO	2	0.589

wide mass range by a next-to-leading order fit in the scaling variable, cf. table 2,

$$\beta_c(am, N_f(N_\tau), N_\tau) = \beta_{\text{tric}}(N_\tau) + \mathcal{C}_1(N_\tau)(am)^{2/5} + \mathcal{C}_2(N_\tau)(am)^{4/5} + \mathcal{O}\left((am)^{6/5}\right). \quad (8)$$

As explained in section 2, a projection of the chiral critical surface onto a plane containing  $N_f$  must necessarily terminate in a tricritical point. For this reason the fit ansatz used here is justified, even though the leading term is just beginning to be constrained.<sup>3</sup>

Next, the  $(am, N_f)$ -plane is shown in figure 4b, which corresponds to the schematic picture from figure 2. The lines correspond to fits according to the scaling relation,

$$N_f^c(am, N_\tau) = N_f^{\text{tric}}(N_\tau) + \mathcal{D}_1(N_\tau)(am)^{2/5} + \mathcal{D}_2(N_\tau)(am)^{4/5} + \mathcal{O}\left((am)^{6/5}\right). \quad (9)$$

For comparison, we have also included the previous  $\mu_i = 0$  data from ref. [12] in this figure. We observe that in both cases the tricritical point, in which the critical line terminates, is strongly cutoff-dependent and moves towards larger  $N_f$ -values as the lattice is made finer, cf. table 3. Given this qualitative similarity, there is an interesting quantitative detail in the comparison. On the coarsest  $N_\tau = 4$  lattices, the first-order region for finite  $\mu_i$  extends to larger bare quark masses than in the case  $\mu_i = 0$ , in agreement with earlier studies using staggered fermions on  $N_\tau = 4$  [44, 45, 46]. However, on the  $N_\tau \in \{6, 8\}$  lattices this situation changes and the  $\mu_i = 0$  data show the larger first-order region, which is consistent with the Wilson study on  $N_\tau = 6$  quoted earlier [47]. This is clear evidence for a mixing of cutoff and finite density effects in the parameter region where we are operating, which is not surprising: we are not yet close to the continuum, nor is our chosen  $\mu_i/T$ -value small.

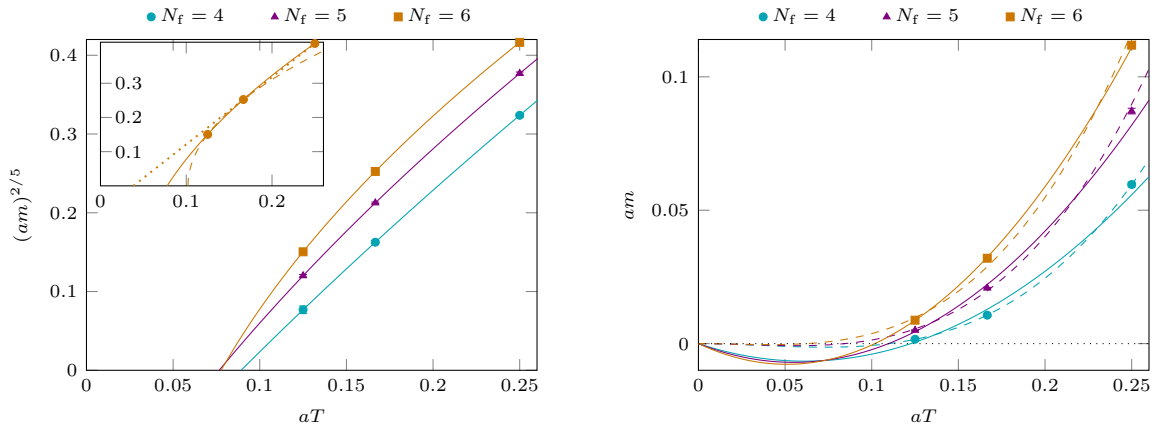
Finally, we project the chiral critical surface on the  $(am, aT = N_\tau^{-1})$ -plane in figure 5a. Once again, the observed behaviour is completely analogous to the case at zero density. The second-order boundary line between the first-order and crossover regions is well described by next-to-leading order tricritical scaling of temperature in terms of the scaling field,

$$(aT)_c(am, N_f) = (aT)_{\text{tric}}(N_f) + E_1(N_f)(am)^{2/5} + E_2(N_f)(am)^{4/5} + \mathcal{O}\left((am)^{6/5}\right). \quad (10)$$

With only three  $N_\tau$ -values available so far, a full next-to-leading order fit is not feasible. The lines in figure 5a thus represent interpolations including LO and NLO terms. Note that for

<sup>3</sup>It is easy to check that a description by a polynomial in terms of  $am$  instead of the scaling field is indeed significantly worse, quantitatively.





(a) Tricritical scaling interpolations (eq. (10)). The inset shows LO (dotted) and NLO (dashed) interpolations for  $N_f = 6$  for an error estimate of  $(aT)_{\text{tric}}$ .

(b) Polynomial fits. Solid lines correspond to LO+NLO fits and dashed lines to NLO+NNLO fits. Fits correspond to eq. (11) with the fit results in table 4.

Figure 5: Critical line for different  $N_f$  in the  $(am, aT)$ -plane.

Table 4: Fit coefficients of the fits from eq. (11) to the data in figure 5b.

$N_f$	$\tilde{F}_3(N_f)$	$\tilde{F}_2(N_f)$	$\tilde{F}_1(N_f)$	fit form	d.o.f.	$\chi^2_{\text{d.o.f.}}$
4.0	—	1.8(3)	-0.21(5)	LO+NLO	1	76.4
	6.81(4)	-0.749(8)	—	NLO+NNLO	1	0.0578
5.0	—	2.33(25)	-0.26(4)	LO+NLO	1	63.1
	8.7(9)	-0.73(15)	—	NLO+NNLO	1	31.2
6.0	—	2.99(5)	-0.305(7)	LO+NLO	1	1.87
	10.0(1.9)	-0.6(3)	—	NLO+NNLO	1	119

fixed  $N_f$  there is no guarantee for a tricritical point to exist in this plane: if the theory with a given  $N_f$  features a first-order transition in the continuum, the  $Z_2$ -boundary line must enter the continuum limit  $(am, aT) = (0, 0)$  without tricritical scaling, i.e. as an ordinary polynomial

$$am_c(N_\tau, N_f) = \tilde{F}_1(N_f) aT + \tilde{F}_2(N_f) (aT)^2 + \tilde{F}_3(N_f) (aT)^3 + \mathcal{O}((aT)^4). \quad (11)$$

As figure 5b and table 4 show, this functional behaviour is incompatible with the data. Instead, the data are fully compatible with the tricritical scaling behaviour observed in the other planes of bare parameter pairings, and hence with the existence of a tricritical line  $N_f^{\text{tric}}(N_\tau)$ , viz.  $N_f^{\text{tric}}(N_f)$  in the lattice chiral limit,  $am = 0$ .

Our findings imply that, just as for zero density, there is a maximal  $N_\tau$  beyond which the first-order transition observed in our simulations is lost, i.e., it is not connected to the continuum limit and thus must be considered a lattice artefact. Since the tricritical point marks a change from first- to second-order behaviour in the lattice chiral limit, the continuum chiral limit corresponds to a second-order transition. The Columbia plot for  $\mu_i = 0.81\pi T/3$  then looks qualitatively the same as in figure 1b.

## 5 Conclusions

We have obtained fully non-perturbative information on the nature of the QCD chiral transition as a function of the theory's parameters, as predicted by lattice QCD using the standard staggered discretisation on  $N_\tau \in \{4, 6, 8\}$  lattices. Both for zero [12] and fixed imaginary chemical

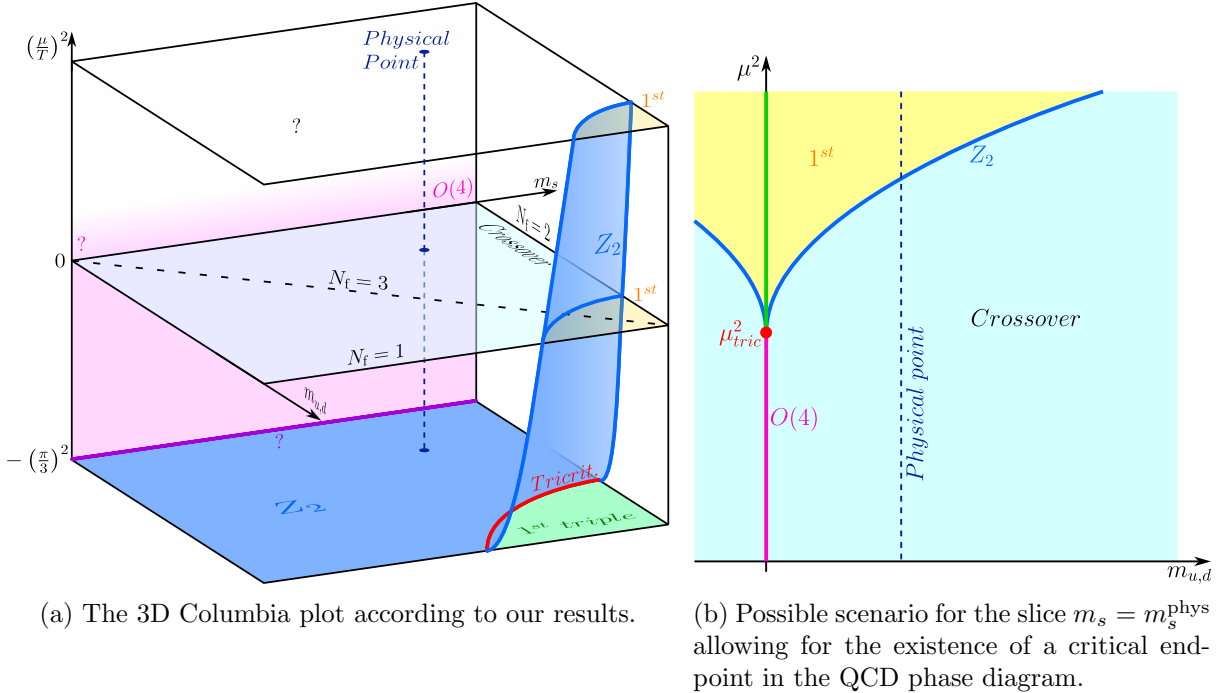


Figure 6

potential, previously observed first-order transition regions vanish before the continuum limit is reached. Unless additional (and so far unobserved) first-order transitions will appear on finer lattices or with chiral fermions, this implies:

- The thermal chiral phase transition of  $N_f = 2 + 1$  QCD is of second order for  $m_{u,d} = 0$  and any value of  $m_s$ , turning into an analytic crossover as soon as  $m_{u,d} \neq 0$ .
- The order of the chiral phase transition in  $N_f = 2 + 1$  QCD does not show any dependence on imaginary chemical potential.

This emerging picture is consistent with the absence of non-analytic chiral transitions in the Roberge-Weiss plane as observed with  $N_f = 2 + 1$  improved staggered fermion actions for  $m_\pi \gtrsim 45\text{MeV}$  [48, 49], and also with results from a particular truncation of DSEs in the continuum at real and imaginary chemical potentials [32, 34]. According to the latter works, the chiral critical surface is analytic around  $\mu = 0$  and remains in the  $m_{u,d} = 0$  plane also for small real chemical potentials. Combining all of this in a 3D Columbia plot, and barring non-monotonic or oscillatory behaviour of the chiral critical surface, the coarse lattice version from figure 3 changes in the continuum limit to the version in figure 6a.

On the other hand, the DSEs in [34] predict the chiral critical surface to bend away from the chiral limit at large real chemical potentials, in accordance with critical point predictions from functional studies [55, 56]. This scenario requires non-analytic behaviour of the chiral critical surface itself as sketched in figure 6b, which represents a possible scenario for the slice  $m_s = m_s^{\text{phys}}$  of the 3D Columbia plot. A tricritical point at finite  $\mu$  in the chiral limit  $m_{u,d} = 0$  has indeed been surmised long ago [3], based on analogies with various models for the chiral phase transition. When the strange quark mass is varied, such a point traces out a tricritical line. Based on low energy effective models and early lattice results, this line was inferred to be continuously connected to the tricritical strange quark mass  $m_s^{\text{tric}}(\mu = 0)$  in the putative Columbia plot figure 1a [2, 4, 5, 6]. Our results, as well as all presently available data from other discretisations and DSE results, are incompatible with this particular scenario and the low energy models predicting it.

In view of the reduced chiral symmetry of staggered fermions, it would be most valuable to perform similar studies with chirally symmetric discretisations, as well as to investigate the quark mass dependence of the critical point observed in Dyson-Schwinger [55] and functional renormalisation group [56] studies.

## Acknowledgements

We acknowledge the help of Alessandro Sciarra to adapt the BaHaMAS software [51] to simulations with imaginary chemical potential, and moving to container-based simulation runs on the supercomputer. We also thank the staff of the VIRGO cluster at GSI Darmstadt, where all simulations have been performed.

We acknowledge use of the unpublished analysis software packages “Monte Carlo Cpp analysis tools” by A. Sciarra, C. Pinke, D. Leemueller et al. and “PLASMA” by C. Pinke, F. Cuteri, A. Sciarra et al. as well as the bash utilities repository “Script” by A. Sciarra, C. Czaban, F. Cuteri et al.

This work is supported by the Deutsche Forschungsgemeinschaft (DFG) through the grant CRC-TR 211 “Strong-interaction matter under extreme conditions” and by the State of Hesse within the Research Cluster ELEMENTS (Project ID 500/10.006). Alfredo D’Ambrosio and Reinhold Kaiser acknowledge support by the Helmholtz Graduate School for Hadron and Ion Research (HGS-HIRe).

## A Simulation statistics

In tables 5, 6 and 7 we provide an overview of the simulations and the accumulated statistics for the three simulated values of  $N_\tau \in \{4, 6, 8\}$ , respectively.

The super-columns report on the different aspect ratios  $N_\sigma/N_\tau$ , which we simulated. Within these super-columns, each line corresponds to a fixed set of lattice parameters  $\{N_\tau, N_f, am, N_\sigma\}$ , which encompasses simulations from several  $\beta$  values and 4 independent Markov chains per  $\beta$ . The first entry  $\beta_{pc}$  is the pseudo-critical gauge coupling determining the phase boundary, which is obtained from the condition of the vanishing skewness. Total statistics sums up the number of all generated and analysed trajectories for all  $\beta$  values of that volume  $N_\sigma$ . Next, the number of simulated  $\beta$  values is reported. To check that simulations have been performed on both sides of the phase boundary, the quantity  $|B_3/\sigma_{B_3}|^{\text{edge}}$  is evaluated on the reweighted data. It measures the distance of the  $B_3$  value at the edge of the simulation range from zero, expressed in units of the standard deviation of  $B_3$ . In the tables we report the minimum value obtained from both edges  $\min(|B_3/\sigma_{B_3}|^{\text{edge}})$  and we use the values at the peaks of  $B_3$ , if the behavior of  $B_3$  is non-monotonous in the simulation range. To ensure with high confidence that the simulation range includes the transition point, we typically require  $\min(|B_3/\sigma_{B_3}|^{\text{edge}}) > 3$ . Finally, we calculate the average distance of the  $B_4$  values for different Markov chains in units of the expectation value of the average distance  $\bar{n}_d(B_4)$ . We report the maximum value  $\max(\bar{n}_d(B_4))$  obtained from different  $\beta$  values for each parameter set  $\{N_\tau, N_f, am, N_\sigma\}$ . In the limit of infinite length of the Markov chain,  $\bar{n}_d(B_4)$  approaches 1. In practice we demand  $\bar{n}_d(B_4)$  to be not much larger than 2.

Table 5: Simulation statistics for  $N_\tau = 4$ .

$N_f$	$am$	$\beta_{pc}$	Total statistics						# $\beta$ values				$\min( B_3/\sigma_{B_3} ^{edge})$				$\max(\bar{n}_d(B_4))$				
			Aspect ratio 3			Aspect ratio 4			Aspect ratio 5				Aspect ratio 6								
1.8	0.0014	5.31470	520k	2	1.7	1.7	5.31495	560k	2	11	1.4										
	0.0017	5.31530	600k	2	13	1.3	5.31545	560k	2	12	2.0	5.31515	600k	2	8.2	1.8					
	0.0020	5.31525	520k	2	6.5	1.9	5.31585	732k	3	14	1.5	5.31555	580k	3	12	1.8					
	0.0023	5.31620	600k	2	15	0.6	5.31600	787k	3	15	1.4	5.31620	480k	2	9.0	1.9					
	0.0026	5.31700	600k	2	13	0.8	5.31650	600k	2	8.6	2.6	5.31680	480k	2	7.1	2.1	5.31700	467k	2	6.1	2.0
	0.0038	5.31945	560k	3	18	1.6	5.31930	440k	2	2.6	1.5	5.31885	480k	2	9.8	1.4	5.31885	180k	2	7.9	2.4
0.0050	5.32155	520k	2	10	1.4	5.32135	440k	2	7.4	1.2	5.32120	540k	2	12	1.9	5.32110	236k	2	6.4	1.2	
$N_f$	$am$	$\beta_{pc}$	Total statistics				# $\beta$ values				$\min( B_3/\sigma_{B_3} ^{edge})$				$\max(\bar{n}_d(B_4))$						
			Aspect ratio 2				Aspect ratio 3				Aspect ratio 4										
1.9	0.0020	5.29495	400k	2	7.0	2.0	5.29835	600k	2	16	1.0	5.29850	640k	3	18	2.1					
	0.0040	5.30255	400k	2	12	2.6	5.30240	400k	2	10	2.0	5.30205	840k	4	16	2.3					
	0.0060	5.30635	400k	2	12	1.3	5.30630	920k	2	21	3.3	5.30550	400k	2	14	2.0					
2.0	0.0040	5.28480	400k	2	14	2.4	5.28535	800k	4	19	1.6	5.28535	400k	2	12	1.8					
	0.0080	5.29355	400k	2	11	1.9	5.29305	400k	2	6.5	2.9	5.29290	800k	4	13	1.2					
	0.0120	5.30035	600k	3	22	1.5	5.30000	400k	2	12	1.8	5.29970	800k	4	19	1.4					
2.1	0.0060	5.27190	400k	2	6.7	1.2	5.27245	600k	3	26	2.0	5.27205	760k	3	20	2.3					
	0.0100	5.28020	400k	2	12	0.84	5.28050	400k	2	11	1.7	5.27975	1.0M	4	15	2.1					
	0.0130	5.28495	400k	2	10	1.1	5.28545	400k	2	14	1.1	5.28530	400k	2	12	1.7					
2.2	0.0080	5.26005	600k	3	26	1.4	5.25870	400k	2	5.8	2.2	5.25935	600k	3	17	1.5					
	0.0110	5.26615	400k	2	13	2.1	5.26530	400k	2	7.2	2.1	5.26495	600k	3	16	1.6					
	0.0140	5.27110	400k	2	14	1.8	5.27055	800k	4	20	2.6	5.27055	800k	4	15	1.7					
2.3	0.0065	5.24070	800k	4	19	2.1	5.24045	360k	2	9.2	1.6										
	0.0110	5.24985	800k	4	22	1.7	5.24905	400k	2	6.9	1.5	5.24900	800k	2	14	2.2					
	0.0170	5.26055	800k	4	25	2.3	5.26035	400k	2	8.7	2.0	5.26005	800k	2	15	1.4					
	0.0230	5.27070	800k	4	24	1.6	5.27055	800k	2	10	2.2	5.27025	800k	2	14	1.7					
3.6	0.0370	5.10820	400k	2	7.0	1.9	5.10760	800k	2	11	1.6	5.10800	1.12M	3	14	3.1					
	0.0420	5.11865	400k	2	5.2	1.7	5.11800	400k	2	8.2	2.0	5.11750	800k	2	6.9	2.4					
	0.0470	5.12790	400k	2	8.8	1.9	5.12765	400k	2	7.9	1.2	5.12705	560k	2	9.8	0.99					
	0.0520	5.13710	400k	2	11	2.1	5.13650	960k	3	19	1.6	5.13645	960k	3	15	1.9					
4.0	0.0500	5.08080	400k	2	4.7	1.9	5.08075	1.2M	3	20	2.2	5.08085	1.2M	4	15	2.4					
	0.0550	5.09075	400k	2	12	2.7	5.09080	600k	3	21	1.6	5.09060	1.4M	3	25	2.1					
	0.0600	5.10075	400k	2	12	1.2	5.10020	1.0M	3	23	1.3	5.10025	1.0M	3	19	1.8					
	0.0650	5.10950	400k	2	8.8	2.0	5.10935	640k	2	16	2.2	5.10930	600k	3	17	1.7					
4.5	0.0650	5.04860	800k	2	7.9	1.7	5.04815	400k	2	8.6	2.0	5.04820	800k	2	8.0	3.8					
	0.0700	5.05815	600k	3	20	2.0	5.05800	600k	3	25	2.6	5.05775	1.1M	4	19	2.0					
	0.0750	5.06735	600k	3	19	1.8	5.06770	600k	3	16	1.8	5.06715	600k	3	14	1.8					
5.0	0.0750	5.00900	800k	4	27	1.9	5.00895	400k	2	13	1.8	5.00910	1.6M	4	17	1.7					
	0.0850	5.02925	800k	4	22	1.8	5.02905	400k	2	12	1.3	5.02875	800k	2	10	1.1					
	0.0950	5.04805	800k	4	27	2.4	5.04755	400k	2	12	1.2	5.04770	800k	2	15	0.99					
	0.1050	5.06605	400k	2	8.1	1.7	5.06575	400k	2	11	1.1	5.06555	800k	2	11	2.2					
6.0	0.1000	4.94985	800k	4	21	2.1	4.95010	400k	2	10	2.7	4.95000	1.6M	4	19	1.7					
	0.1150	4.98020	800k	2	1.6	1.0	4.98025	400k	2	11	1.8	4.97980	800k	2	14	1.4					
	0.1300	5.00830	400k	2	7.5	1.5	5.00785	400k	2	10	2.0	5.00800	800k	2	9.8	2.6					

Table 6: Simulation statistics for  $N_\tau = 6$ .

$N_f$	$am$	$\beta_{pc}$	Total statistics					# $\beta$ values		$\min( B_3/\sigma_{B_3} ^{edge})$			$\max(\bar{n}_d(B_4))$				
			Aspect ratio 2					Aspect ratio 3					Aspect ratio 4				
3.0	0.0010	5.22400	360k	3	13	2.7	5.22510	560k	3	16	1.7						
	0.0020	5.22860	240k	2	9.4	1.8	5.22905	364k	2	6.8	2.0	5.22850	560k	3	10	1.6	
	0.0030	5.23330	240k	2	7.9	1.9	5.23290	464k	2	9.9	2.1	5.23285	680k	4	16	1.7	
3.3	0.0030	5.18145	240k	2	7.7	1.9	5.18205	560k	2	10	1.5	5.18195	1.04M	3	11	3.7	
	0.0045	5.18840	280k	2	5.0	1.3	5.18850	1.04M	3	14	2.7	5.18845	1.0M	4	14	1.4	
	0.0060	5.19475	400k	2	12	1.2	5.19520	600k	3	13	1.6	5.19485	660k	2	8.0	1.6	
	0.0075	5.20060	400k	2	12	1.5	5.20080	400k	2	4.4	1.3	5.20090	600k	3	4.9	1.7	
3.6	0.0050	5.14120	880k	3	17	1.2	5.14125	1.2M	3	12	1.9	5.14115	1.1M	3	7.4	2.0	
	0.0075	5.15245	400k	2	10	1.0	5.15205	600k	3	13	1.6	5.15170	880k	3	14	1.9	
	0.0100	5.16195	400k	2	6.7	1.4	5.16205	1.02M	3	14	1.7	5.16195	600k	3	11	1.8	
4.0	0.0075	5.08810	400k	2	6.1	1.8	5.08810	1.06M	3	11	1.6	5.08820	1.2M	3	23	4.7	
	0.0100	5.09810	400k	2	9.6	3.0	5.09850	1.0M	3	24	0.87	5.09825	800k	4	17	1.5	
	0.0125	5.10865	400k	2	12	0.52	5.10855	800k	4	18	1.9	5.10850	840k	3	6.8	1.6	
4.5	0.0100	5.02150	560k	2	2.8	1.1	5.02195	1.04M	3	20	1.5	5.02260	1.6M	5	32	2.5	
	0.0140	5.03815	840k	3	20	1.8	5.03800	1.08M	3	17	2.5	5.03825	1.2M	4	9.8	3.4	
	0.0180	5.05365	400k	2	5.3	2.2	5.05375	600k	3	17	1.9	5.05360	1.06M	3	12	2.2	
5.0	0.0175	4.97865	800k	4	23	1.6	4.97855	1.6M	4	21	3.1	4.97850	1.2M	4	18	3.6	
	0.0210	4.99170	400k	2	10	1.4	4.99230	560k	2	7.4	2.1	4.99220	1.2M	4	13	2.0	
	0.0250	5.00680	1.28M	4	19	2.7	5.00755	400k	2	7.3	1.2	5.00725	1.6M	4	13	1.6	
6.0	0.0300	4.88800	400k	2	9.8	1.8	4.88838	800k	4	20	2.4	4.88834	1.6M	4	11	4.8	
	0.0340	4.90350	400k	2	6.7	1.2	4.90340	400k	2	8.5	1.4	4.90358	1.2M	4	15	3.0	
	0.0380	4.91790	400k	2	8.5	1.4	4.91815	400k	2	8.6	1.4	4.91860	960k	2	3.1	0.85	

Table 7: Simulation statistics for  $N_\tau = 8$ .

$N_f$	$am$	$\beta_{pc}$	Total statistics					# $\beta$ values		$\min( B_3/\sigma_{B_3} ^{edge})$			$\max(\bar{n}_d(B_4))$				
			Aspect ratio 2					Aspect ratio 3					Aspect ratio 4				
4.0	0.0010	5.10788	180k	2	8.0	1.7											
	0.0015	5.11150	200k	2	8.3	1.6	5.11100	247k	2	5.9	1.2						
	0.0020	5.11485	360k	3	12	1.8	5.11445	440k	2	8.3	1.7						
	0.0025	5.11790	400k	2	9.2	1.9	5.11815	220k	2	7.7	1.0	5.11840	319k	2	3.9	2.4	
	0.0030	5.12190	400k	2	6.4	0.9	5.12185	240k	2	5.5	2.5	5.12200	380k	2	7.5	2.6	
4.5	0.0020	5.02845	760k	4	14	2.3	5.02835	540k	2	9.0	1.1						
	0.0030	5.03585	400k	2	3.3	2.2	5.03590	675k	3	11	1.1	5.03620	373k	2	3.3	0.93	
	0.0040	5.04395	320k	2	3.1	1.4	5.04355	600k	3	7.5	2.8	5.04365	480k	3	8.9	1.6	
5.0	0.0040	4.96050	600k	4	15	1.9	4.96035	800k	2	4.7	3.1						
	0.0050	4.96755	400k	2	9.8	1.3	4.96795	600k	4	13	3.0	4.96775	880k	4	9.9	1.3	
	0.0060	4.97510	680k	4	13	2.4	4.97525	400k	2	7.2	1.6	4.97510	640k	2	1.5	0.85	
	0.0075	4.98560	560k	4	12	1.6	4.98555	400k	2	5.4	1.6	4.98585	400k	2	3.5	1.0	
5.5	0.0050	4.88695	400k	2	14	1.5	4.88715	1.2M	4	9.5	2.9						
	0.0065	4.89785	400k	2	9.3	2.5	4.89810	560k	2	5.0	2.0	4.89810	560k	2	8.1	2.0	
	0.0075	4.90490	680k	3	12	1.9	4.90510	400k	2	5.1	2.5	4.90525	800k	2	4.0	1.2	
6.0	0.0060	4.81595	760k	2	7.2	2.1	4.81650	1.04M	4	44	3.8						
	0.0080	4.83035	960k	4	16	2.4	4.83044	960k	4	18	2.0	4.83048	800k	2	7.6	2.3	
	0.0100	4.84400	400k	2	3.6	1.2	4.84425	800k	2	2.0	2.0	4.84438	560k	3	7.8	1.5	

## References

- [1] Y. Aoki, G. Endrödi, Z. Fodor, S. D. Katz, and K. K. Szabo. The order of the quantum chromodynamics transition predicted by the standard model of particle physics. *Nature*, 443:675–678, 2006. [arXiv:hep-lat/0611014](#), [doi:10.1038/nature05120](#).
- [2] Krishna Rajagopal. The Chiral phase transition in QCD: Critical phenomena and long wavelength pion oscillations. pages 484–554, 4 1995. [arXiv:hep-ph/9504310](#), [doi:10.1142/9789812830661\\_0009](#).
- [3] Adam Miklos Halasz, A. D. Jackson, R. E. Shrock, Misha A. Stephanov, and J. J. M. Verbaarschot. On the phase diagram of QCD. *Phys. Rev. D*, 58:096007, 1998. [arXiv:hep-ph/9804290](#), [doi:10.1103/PhysRevD.58.096007](#).
- [4] Stephen D. H. Hsu and Myckola Schwetz. On the QCD phase transition at finite baryon density. *Phys. Lett. B*, 432:203–208, 1998. [arXiv:hep-ph/9803386](#), [doi:10.1016/S0370-2693\(98\)00615-7](#).
- [5] Misha A. Stephanov, K. Rajagopal, and Edward V. Shuryak. Signatures of the tricritical point in QCD. *Phys. Rev. Lett.*, 81:4816–4819, 1998. [arXiv:hep-ph/9806219](#), [doi:10.1103/PhysRevLett.81.4816](#).
- [6] Krishna Rajagopal and Frank Wilczek. The Condensed matter physics of QCD. In M. Shifman and Boris Ioffe, editors, *At the frontier of particle physics. Handbook of QCD. Vol. 1-3*, pages 2061–2151. 2000. [arXiv:hep-ph/0011333](#), [doi:10.1142/9789812810458\\_0043](#).
- [7] Yoshitaka Hatta and Takashi Ikeda. Universality, the QCD critical / tricritical point and the quark number susceptibility. *Phys. Rev. D*, 67:014028, 2003. [arXiv:hep-ph/0210284](#), [doi:10.1103/PhysRevD.67.014028](#).
- [8] H. T. Ding et al. Chiral Phase Transition Temperature in (2+1)-Flavor QCD. *Phys. Rev. Lett.*, 123(6):062002, 2019. [arXiv:1903.04801](#), [doi:10.1103/PhysRevLett.123.062002](#).
- [9] Andrey Yu. Kotov, Maria Paola Lombardo, and Anton Trunin. QCD transition at the physical point, and its scaling window from twisted mass Wilson fermions. *Phys. Lett. B*, 823:136749, 2021. [arXiv:2105.09842](#), [doi:10.1016/j.physletb.2021.136749](#).
- [10] Robert D. Pisarski and Frank Wilczek. Remarks on the Chiral Phase Transition in Chromodynamics. *Phys. Rev.*, D29:338–341, 1984. [doi:10.1103/PhysRevD.29.338](#).
- [11] Andrea Pelissetto and Ettore Vicari. Relevance of the axial anomaly at the finite-temperature chiral transition in QCD. *Phys. Rev. D*, 88(10):105018, 2013. [arXiv:1309.5446](#), [doi:10.1103/PhysRevD.88.105018](#).
- [12] Francesca Cuteri, Owe Philipsen, and Alessandro Sciarra. On the order of the QCD chiral phase transition for different numbers of quark flavours. *JHEP*, 11:141, 2021. [arXiv:2107.12739](#), [doi:10.1007/JHEP11\(2021\)141](#).
- [13] H. Gausterer and S. Sanielevici. Can the Chiral Transition in QCD Be Described by a Linear  $\sigma$  Model in Three-dimensions? *Phys. Lett. B*, 209:533–537, 1988. [doi:10.1016/0370-2693\(88\)91188-4](#).
- [14] Agostino Butti, Andrea Pelissetto, and Ettore Vicari. On the nature of the finite temperature transition in QCD. *JHEP*, 08:029, 2003. [arXiv:hep-ph/0307036](#), [doi:10.1088/1126-6708/2003/08/029](#).

- [15] Frank R. Brown, Frank P. Butler, Hong Chen, Norman H. Christ, Zhi-hua Dong, Wendy Schaffer, Leo I. Unger, and Alessandro Vaccarino. On the existence of a phase transition for QCD with three light quarks. *Phys. Rev. Lett.*, 65:2491–2494, 1990. doi:10.1103/PhysRevLett.65.2491.
- [16] Y. Iwasaki, K. Kanaya, S. Kaya, S. Sakai, and T. Yoshie. Finite temperature transitions in lattice QCD with Wilson quarks: Chiral transitions and the influence of the strange quark. *Phys. Rev. D*, 54:7010–7031, 1996. arXiv:hep-lat/9605030, doi:10.1103/PhysRevD.54.7010.
- [17] F. Karsch, E. Laermann, and C. Schmidt. The Chiral critical point in three-flavor QCD. *Phys. Lett.*, B520:41–49, 2001. arXiv:hep-lat/0107020, doi:10.1016/S0370-2693(01)01114-5.
- [18] Philippe de Forcrand and Owe Philipsen. The QCD phase diagram for three degenerate flavors and small baryon density. *Nucl. Phys.*, B673:170–186, 2003. arXiv:hep-lat/0307020, doi:10.1016/j.nuclphysb.2003.09.005.
- [19] Owe Philipsen. Lattice Constraints on the QCD Chiral Phase Transition at Finite Temperature and Baryon Density. *Symmetry*, 13(11):2079, 2021. arXiv:2111.03590, doi:10.3390/sym13112079.
- [20] Anirban Lahiri. Aspects of finite temperature QCD towards the chiral limit. *PoS, LATTICE2021:003*, 2022. arXiv:2112.08164, doi:10.22323/1.396.0003.
- [21] Jana N. Guenther. An overview of the QCD phase diagram at finite  $T$  and  $\mu$ . *PoS, LATTICE2021:013*, 2022. arXiv:2201.02072, doi:10.22323/1.396.0013.
- [22] Yoshinobu Kuramashi, Yoshifumi Nakamura, Hiroshi Ohno, and Shinji Takeda. Nature of the phase transition for finite temperature  $N_f = 3$  QCD with nonperturbatively  $O(a)$  improved Wilson fermions at  $N_t = 12$ . *Phys. Rev. D*, 101(5):054509, 2020. arXiv:2001.04398, doi:10.1103/PhysRevD.101.054509.
- [23] Lorenzo Dini, Prasad Hegde, Frithjof Karsch, Anirban Lahiri, Christian Schmidt, and Sipaz Sharma. Chiral phase transition in three-flavor QCD from lattice QCD. *Phys. Rev. D*, 105(3):034510, 2022. arXiv:2111.12599, doi:10.1103/PhysRevD.105.034510.
- [24] Yu Zhang, Yasumichi Aoki, Shoji Hashimoto, Issaku Kanamori, Takashi Kaneko, and Yoshifumi Nakamura. Finite temperature QCD phase transition with 3 flavors of Möbius domain wall fermions. *PoS, LATTICE2022:197*, 2023. arXiv:2212.10021, doi:10.22323/1.430.0197.
- [25] Yu Zhang, Yasumichi Aoki, Shoji Hashimoto, Issaku Kanamori, Takashi Kaneko, and Yoshifumi Nakamura. Three flavor QCD phase transition with Möbius domain wall fermions. *PoS, LATTICE2024:193*, 2025. arXiv:2501.15494, doi:10.22323/1.466.0193.
- [26] Yu Zhang, Yasumichi Aoki, Shoji Hashimoto, Issaku Kanamori, Takashi Kaneko, and Yoshifumi Nakamura. Exploring the QCD phase diagram with three flavors of Möbius domain wall fermions. *PoS, LATTICE2023:203*, 2024. arXiv:2401.05066, doi:10.22323/1.453.0203.
- [27] G. Fejos. Second-order chiral phase transition in three-flavor quantum chromodynamics? *Phys. Rev. D*, 105(7):L071506, 2022. arXiv:2201.07909, doi:10.1103/PhysRevD.105.L071506.



- [28] Robert D. Pisarski and Fabian Rennecke. Conjectures about the Chiral Phase Transition in QCD from Anomalous Multi-Instanton Interactions. *Phys. Rev. Lett.*, 132(25):251903, 2024. [arXiv:2401.06130](#), [doi:10.1103/PhysRevLett.132.251903](#).
- [29] Francesco Giacosa, Győző Kovács, Péter Kovács, Robert D. Pisarski, and Fabian Rennecke. Anomalous U(1)A couplings and the Columbia plot. *Phys. Rev. D*, 111(1):016014, 2025. [arXiv:2410.08185](#), [doi:10.1103/PhysRevD.111.016014](#).
- [30] G. Fejos and T. Hatsuda. Order of the SU(Nf)×SU(Nf) chiral transition via the functional renormalization group. *Phys. Rev. D*, 110(1):016021, 2024. [arXiv:2404.00554](#), [doi:10.1103/PhysRevD.110.016021](#).
- [31] Stefanos Robert Kousvos and Andreas Stergiou. CFTs with  $U(\mathbf{m}) \times U(\mathbf{n})$  global symmetry in 3D and the chiral phase transition of QCD. *SciPost Phys.*, 15(2):075, 2023. [arXiv:2209.02837](#), [doi:10.21468/SciPostPhys.15.2.075](#).
- [32] Julian Bernhardt and Christian S. Fischer. QCD phase transitions in the light quark chiral limit. *Phys. Rev. D*, 108(11):114018, 2023. [arXiv:2309.06737](#), [doi:10.1103/PhysRevD.108.114018](#).
- [33] Alfredo D’Ambrosio, Owe Philipsen, and Reinhold Kaiser. The chiral phase transition at non-zero imaginary baryon chemical potential for different numbers of quark flavours. *PoS, LATTICE2022:172*, 2023. [arXiv:2212.03655](#), [doi:10.22323/1.430.0172](#).
- [34] Julian Bernhardt and Christian S. Fischer. Quark mass dependence of a QCD critical point and structure of the Columbia plot. 7 2025. [arXiv:2507.21680](#).
- [35] Francesca Cuteri, Owe Philipsen, and Alessandro Sciarra. QCD chiral phase transition from noninteger numbers of flavors. *Phys. Rev. D*, 97(11):114511, 2018. [arXiv:1711.05658](#), [doi:10.1103/PhysRevD.97.114511](#).
- [36] I.D. Lawrie and S. Sarbach. Theory of tricritical points. In C. Domb and J.L. Lebowitz, editors, *Phase transitions and critical phenomena*, volume 9, page 1. 1984.
- [37] Andre Roberge and Nathan Weiss. Gauge Theories With Imaginary Chemical Potential and the Phases of QCD. *Nucl. Phys. B*, 275:734–745, 1986. [doi:10.1016/0550-3213\(86\)90582-1](#).
- [38] Alessandro Sciarra. *The QCD phase diagram at purely imaginary chemical potential from the lattice*. PhD thesis, Goethe U., Frankfurt (Main), 2016.
- [39] Owe Philipsen and Alessandro Sciarra. Finite Size and Cut-Off Effects on the Roberge-Weiss Transition in  $N_f = 2$  QCD with Staggered Fermions. *Phys. Rev. D*, 101(1):014502, 2020. [arXiv:1909.12253](#), [doi:10.1103/PhysRevD.101.014502](#).
- [40] Owe Philipsen and Christopher Pinke. The  $N_f = 2$  QCD chiral phase transition with Wilson fermions at zero and imaginary chemical potential. *Phys. Rev.*, D93(11):114507, 2016. [arXiv:1602.06129](#), [doi:10.1103/PhysRevD.93.114507](#).
- [41] Christopher Czaban, Francesca Cuteri, Owe Philipsen, Christopher Pinke, and Alessandro Sciarra. Roberge-Weiss transition in  $N_f = 2$  QCD with Wilson fermions and  $N_\tau = 6$ . *Phys. Rev.*, D93(5):054507, 2016. [arXiv:1512.07180](#), [doi:10.1103/PhysRevD.93.054507](#).
- [42] Philippe de Forcrand and Owe Philipsen. Constraining the QCD phase diagram by tricritical lines at imaginary chemical potential. *Phys. Rev. Lett.*, 105:152001, 2010. [arXiv:1004.3144](#), [doi:10.1103/PhysRevLett.105.152001](#).

- [43] Claudio Bonati, Guido Cossu, Massimo D’Elia, and Francesco Sanfilippo. Roberge-weiss endpoint in  $N_f = 2$  qcd. *Phys. Rev. D*, 83:054505, Mar 2011. URL: <http://link.aps.org/doi/10.1103/PhysRevD.83.054505>, doi:10.1103/PhysRevD.83.054505.
- [44] Philippe de Forcrand and Owe Philipsen. The Chiral critical line of  $N_f = 2 + 1$  QCD at zero and non-zero baryon density. *JHEP*, 0701:077, 2007. [arXiv:hep-lat/0607017](https://arxiv.org/abs/hep-lat/0607017), doi:10.1088/1126-6708/2007/01/077.
- [45] Philippe de Forcrand, Seyong Kim, and Owe Philipsen. A QCD chiral critical point at small chemical potential: Is it there or not? *PoS, LAT2007:178*, 2007. [arXiv:0711.0262](https://arxiv.org/abs/0711.0262).
- [46] Philippe de Forcrand and Owe Philipsen. The Chiral critical point of  $N_f = 3$  QCD at finite density to the order  $(\mu/T)^4$ . *JHEP*, 11:012, 2008. [arXiv:0808.1096](https://arxiv.org/abs/0808.1096), doi:10.1088/1126-6708/2008/11/012.
- [47] Xiao-Yong Jin, Yoshinobu Kuramashi, Yoshifumi Nakamura, Shinji Takeda, and Akira Ukawa. Curvature of the critical line on the plane of quark chemical potential and pseudoscalar meson mass for three-flavor QCD. *Phys. Rev.*, D92(11):114511, 2015. [arXiv:1504.00113](https://arxiv.org/abs/1504.00113), doi:10.1103/PhysRevD.92.114511.
- [48] Claudio Bonati, Enrico Calore, Massimo D’Elia, Michele Mesiti, Francesco Negro, Francesco Sanfilippo, Sebastiano Fabio Schifano, Giorgio Silvi, and Raffaele Tripiccion. Roberge-Weiss endpoint and chiral symmetry restoration in  $N_f = 2 + 1$  QCD. *Phys. Rev. D*, 99(1):014502, 2019. [arXiv:1807.02106](https://arxiv.org/abs/1807.02106), doi:10.1103/PhysRevD.99.014502.
- [49] F. Cuteri, J. Goswami, F. Karsch, Anirban Lahiri, M. Neumann, O. Philipsen, Christian Schmidt, and A. Sciarra. Toward the chiral phase transition in the Roberge-Weiss plane. *Phys. Rev. D*, 106(1):014510, 2022. [arXiv:2205.12707](https://arxiv.org/abs/2205.12707), doi:10.1103/PhysRevD.106.014510.
- [50] Alessandro Sciarra, Christopher Pinke, Matthias Bach, Francesca Cuteri, Lars Zeidlewicz, Christian Schäfer, Tim Breitenfelder, Christopher Czaban, Stefano Lottini, and Paul Frederik Depta. Cl2qcd, February 2021. doi:10.5281/zenodo.5121917.
- [51] Alessandro Sciarra. Bahamas, February 2021. doi:10.5281/zenodo.4577425.
- [52] A. M. Ferrenberg and R. H. Swendsen. New Monte Carlo Technique for Studying Phase Transitions. *Phys. Rev. Lett.*, 61:2635–2638, 1988. doi:10.1103/PhysRevLett.61.2635.
- [53] H. W. J. Blote, E. Luijten, and J. R. Heringa. Ising universality in three dimensions: a Monte Carlo study. *J. Phys. A*, 28(22):6289–6313, 1995. [arXiv:cond-mat/9509016](https://arxiv.org/abs/cond-mat/9509016), doi:10.1088/0305-4470/28/22/007.
- [54] Andrea Pelissetto and Ettore Vicari. Critical phenomena and renormalization group theory. *Phys. Rept.*, 368:549–727, 2002. [arXiv:cond-mat/0012164](https://arxiv.org/abs/cond-mat/0012164), doi:10.1016/S0370-1573(02)00219-3.
- [55] Christian S. Fischer. QCD at finite temperature and chemical potential from Dyson–Schwinger equations. *Prog. Part. Nucl. Phys.*, 105:1–60, 2019. [arXiv:1810.12938](https://arxiv.org/abs/1810.12938), doi:10.1016/j.pnpnp.2019.01.002.
- [56] Fei Gao and Jan M. Pawłowski. Chiral phase structure and critical end point in QCD. *Phys. Lett. B*, 820:136584, 2021. [arXiv:2010.13705](https://arxiv.org/abs/2010.13705), doi:10.1016/j.physletb.2021.136584.